Supplementary Information for

Spatial Information Lasing Enabled by Full-*k*-space Bound States in the Continuum

Authors: Ruoheng Chai[1], Wenwei Liu[1,*], Zhancheng Li[1], Yuebian Zhang[1], Haonan Wang[1], Hua Cheng[1,*], Jianguo Tian[1], and Shuqi Chen[1,2,3,*]

Affiliations:
[1]The Key Laboratory of Weak Light Nonlinear Photonics, Ministry of Education, School of Physics and TEDA Institute of Applied Physics, Nankai University, Tianjin 300071, China

[2]School of Materials Science and Engineering, Smart Sensing Interdisciplinary Science Center, Nankai University, Tianjin 300350, China

[3]The Collaborative Innovation Center of Extreme Optics, Shanxi University, Taiyuan 030006, China

*Corresponding authors. Email: Wenwei Liu: wliu@nankai.edu.cn, Hua Cheng: hcheng@nankai.edu.cn, Shuqi Chen: schen@nankai.edu.cn

This PDF file includes:

Supplementary Sections I-VIII

Supplementary Figs. S1 to S11

Supplementary Table. S1

I. Dispersion relations of the 1st-order sinusoidal PTMMs

In the vicinity of the second stopband (the Γ point) and under the diffraction limit, the one dimensional (1D) wave equation:

$$\left(\frac{\partial^2}{\partial x^2}+\frac{\partial^2}{\partial z^2}\right)E_y(x,z)+\varepsilon(x,z)k_0^2E_y(x,z)=0 \tag{S1}$$

is solved by the approximated electric field distributions $E_y(x,z)$ (TE-like modes) and the dielectric constant $\varepsilon(x,z)$ of the 1st-order sinusoidal PTMMs (structure in Fig. 2) [1], given by

$$E_y(x,z)=\left(A(x)e^{+iKx}+B(x)e^{-iKx}\right)\varphi(z)+E_{rad}^0, \tag{S2}$$

and

$$\begin{aligned}\varepsilon(x,z)&=\varepsilon_0(z)+\varepsilon_{PT}(z)\left[\cos(Kx)-iV_0\sin(Kx)\right]\\&=\varepsilon_0(z)+\varepsilon_{+1}(z)e^{+iKx}+\varepsilon_{-1}(z)e^{-iKx}\end{aligned}, \tag{S3}$$

where $\varepsilon_{\pm1}(z)=\frac{1\mp V_0}{2}\varepsilon_{PT}(z)$. After substituting equations (S2) and (S3) into equation (S1) and collecting the items with the same exponents $e^{inKx}(n=0,\pm1)$, we get three coupled equations about the guided waves and the radiating wave:

$$\left[\frac{\partial^2}{\partial z^2}+(K\Omega)^2\varepsilon_0(z)\right]E_0^{rad}=-(K\Omega)^2\left[\varepsilon_{-1}(z)A(x)+\varepsilon_{+1}(z)B(x)\right]\varphi(z), \tag{S4}$$

$$\left[\frac{\partial^2}{\partial z^2}+(K\Omega)^2\varepsilon_0(z)-K^2+2iK\frac{\partial}{\partial x}\right]A(x)\varphi(z)=-(K\Omega)^2\varepsilon_{+1}(z)E_{rad}^0, \tag{S5}$$

$$\left[\frac{\partial^2}{\partial z^2}+(K\Omega)^2\varepsilon_0(z)-K^2-2iK\frac{\partial}{\partial x}\right]B(x)\varphi(z)=-(K\Omega)^2\varepsilon_{-1}(z)E_{rad}^0. \tag{S6}$$

Here, we used $k_0=K\Omega$. A slowly varying approximation of $A(x)=Ae^{-ik_xx}$ and $B(x)=Be^{-ik_xx}$ was employed in order to drop the second order derivative terms $\partial^2A(x)/\partial^2x$ and $\partial^2B(x)/\partial^2x$. Equation (S4) can be solved in terms of Green's function $G(z,z')$, given by

$$E_{rad}^{0}(x,z) = -(K\Omega)^2 \int_{-\infty}^{+\infty} G(z,z')\left[\varepsilon_{-1}(z')A(x) + \varepsilon_{+1}(z')B(x)\right]\varphi(z')dz'. \tag{S7}$$

In the vicinity of the second stopband center Ω_0, $\varphi(z)e^{iKx}$ is the solution of equation (S1) for a homogeneous waveguide, satisfying

$$\left[\frac{\partial^2}{\partial z^2} + (K\Omega_0)^2\varepsilon_0(z) - K^2\right]\varphi(z) = 0. \tag{S8}$$

By substituting equations (S7) and (S8) into equations (S4)–(S6) and employing the normalization condition $\int_{-\infty}^{+\infty} \varphi^*(z)\varphi(z)dz = 1$, we get the coupling equations of the two counter-propagating guided waves:

$$\begin{bmatrix} (\Delta\Omega K)h_0 + ih_1^2 - k_x & ih_{+1}^2 \\ ih_{-1}^2 & (\Delta\Omega K)h_0 + ih_1^2 + k_x \end{bmatrix}\begin{bmatrix} A \\ B \end{bmatrix} = 0, \tag{S9}$$

in which, we used $\Delta\Omega = \Omega - \Omega_0 \approx \frac{\Omega^2 - \Omega_0^2}{2\Omega}$ and the coupling coefficients are given by

$$h_0 = \Omega\int_{-t}^{0} \varepsilon_0(z)\varphi^*(z)\varphi(z)dy, \tag{S10}$$

$$h_1^2 = i\frac{K^3\Omega^4}{8}(1-V_0^2)\varepsilon_{PT}^2\int_{-t}^{0}\int_{-t}^{0} \varepsilon_0(z)\varphi^*(z)\varphi(z)dy, \tag{S11}$$

$$h_{\pm1}^2 = i\frac{K^3\Omega^4}{8}(1\pm V_0)^2\varepsilon_{PT}^2\int_{-t}^{0}\int_{-t}^{0} \varepsilon_0(z)\varphi^*(z)\varphi(z)dy. \tag{S12}$$

Solving equation (S9), we obtain the dispersion relations:

$$\Omega(k_x) = \Omega_0 + \frac{-ih_1^2 \pm \sqrt{k_x^2 - h_{+1}^2h_{-1}^2}}{Kh_0}. \tag{S13}$$

The complex bands (Riemann surface) are obtained by fitting simulation data via equation (S13), as shown in Fig. S1. We get the Dirac cone dispersions when $V_0 = 1$:

$$\Omega(k_x) = \Omega_0 \pm \frac{k_x}{Kh_0}. \tag{S14}$$

Note that the bands are purely real regardless of the wavevector, thus achieving full-*k* BICs. A coincidence of EP and BIC takes place at the Γ point.

Similarly, in the vicinity of the third stopband (the X point, with 0th-, −1st-order diffraction), the approximated electric fields consist of two counter-propagating guided waves and two radiating waves:

$$E_y(x,z)=\left(A(x)e^{+i\frac{3}{2}Kx}+B(x)e^{-i\frac{3}{2}Kx}\right)\varphi(z)+E_{rad}^{0}e^{+i\frac{1}{2}Kx}+E_{rad}^{-1}e^{-i\frac{1}{2}Kx}. \tag{S15}$$

Then the resemble dispersion relations can be obtained:

$$\Omega(k_x)=\Omega_0+\frac{-ih_1^2\pm\sqrt{\left(\frac{3}{2}\left(k_x-\frac{K}{2}\right)\right)^2-h_{+1}^3h_{-1}^3}}{Kh_0}, \tag{S16}$$

in which, the coefficients can be derived in a similar way, with the same scaling laws of V_0 but not exactly the same expressions with equations (S10-12). We get the Dirac cone dispersions when $V_0 = 1$ as well:

$$\Omega(k_x)=\Omega_0\pm\frac{3\left(k_x-\frac{K}{2}\right)}{2Kh_0}. \tag{S17}$$

Note that one obtains full-k BICs and coincidence of EPs and BICs at the X point. In summary, we achieve full-k BICs regardless of radiation channels and EP-BIC coincidence at high-symmetry k-points.

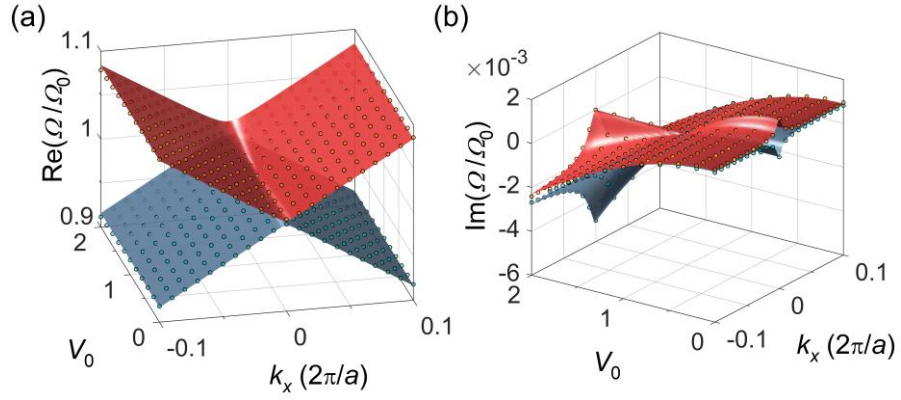

Fig. S1. Riemann surfaces at the 2nd stopband (Γ point) as a function of V_0 and k_x corresponding to the real (a) and imaginary parts (b) of the eigenvalues. Dots, simulations; surfaces, theory.

II. Dispersion relations of the D-PTMM

In the vicinity of the third stopband (X point), the electric field distributions are approximated as:

$$E_y(x,z)=\left(A(x)e^{+i\frac{3}{2}Kx}+B(x)e^{-i\frac{3}{2}Kx}\right)\varphi(z)+E_0^{rad}e^{+i\frac{1}{2}Kx}+E_{-1}^{rad}e^{-i\frac{1}{2}Kx}. \tag{S18}$$

Similarly, we expand the dielectric function $\varepsilon(x,y)$ of the D-PTMM into Fourier series to the 3rd-order, and the non-zero items are given by (corresponding to structures in Fig. 3)

$$\varepsilon(x,z)=\varepsilon_0(z)+\varepsilon_{-1}(z)e^{-iKx}+\varepsilon_{+3}(z)e^{+i3Kx}. \tag{S19}$$

After substituting equations (S18) and (S19) into the 1D Helmholtz equation of equation (S1) and collecting the items with the same exponent, we get four coupled equations about the two guided waves and the two radiating waves. Similarly, the radiating waves are eliminated by the Green's function $G'(y,y')$ and $\varphi(z)e^{i\frac{3}{2}Kx}$ is used as the solution of equation (S1) for a homogeneous waveguide. We finally get the coupled equations of the two counter-propagating guided waves around the X point in the diffraction region (0, –1):

$$\begin{bmatrix}(\Delta\Omega K)h_0-\frac{3}{2}\left(k_x-\frac{1}{2}K\right) & h_{+3}\\ -ih_{-1} & (\Delta\Omega K)h_0+\frac{3}{2}\left(k_x-\frac{1}{2}K\right)\end{bmatrix}\begin{bmatrix}A\\B\end{bmatrix}=0, \tag{S20}$$

in which, $\Delta\Omega=\Omega-\Omega_0\approx\dfrac{\Omega^2-\Omega_0^2}{2\Omega}$ was used as well. The coupling coefficients are expressed as

$$h_0=\Omega\int_{-t}^{0}\varepsilon_0(z)\varphi^*(z)\varphi(z)dy, \tag{S21}$$

$$h_{-1}=i\frac{K^5\Omega^6}{2}\varepsilon_{-1}^3\int_{-t}^{0}\int_{-t}^{0}\int_{-t}^{0}\varphi^*(y)G'(y,y')G'(y',y'')\varphi(y'')dy''dy'dy, \tag{S22}$$

$$h_{+3} = \frac{K\Omega^2}{2}\varepsilon_{+3}\int_{-t}^{0}\varphi^*(y)\varphi(y)dy\,. \tag{S23}$$

Solving equation (S20), we obtain the dispersion relations of the D-PTMM:

$$\Omega(k_x) = \Omega_0 + \frac{\pm\sqrt{\left(\frac{3}{2}\left(k_x - \frac{1}{2}K\right)\right)^2 - ih_{-1}h_{+3}}}{Kh_0}\,. \tag{S24}$$

We fit the simulation results in Fig. 3a by equation (S24) with parameters h_0, h_{-1}, and h_{+3}. The good agreements between simulations and theoretic fittings consolidate that our 3rd-order CFC approximation is sufficient. The bands transform into the Dirac dispersions around the X point when there only exists −1st order complex Fourier component ($h_{+3} = 0$):

$$\Omega(k_x) = \Omega_0 \pm \frac{3\left(k_x - \frac{1}{2}K\right)}{2Kh_0}, \tag{S25}$$

where we obtain full-*k* BICs and the EP-BIC coincident at the high-symmetry *k*-points ($k_x = \frac{1}{2}K$).

III. *Q* factors diverging to infinity

To show the divergence of the simulated *Q* factors to infinity in the full *k*-space, we plot the *Q* factors in the diffraction region 0 and (0, −1) of the sinusoidal PTMMs with only −1st-order CFC (Fig. S2) and with additional high-order CFCs (Fig. S3), respectively. The calculations are accomplished with finite-element-method (FEM) offered by COMSOL Multiphysics. In contrast to general optical FEM simulations of dielectric materials that require the maximum mesh size smaller than λ/6 or λ/8 (λ is the effective wavelength inside the dielectric materials), our simulations of the sinusoidal PTMMs require much finer mesh size because the smoothness of the dielectric functions is necessary for the fill-*k* BICs. The *Q* factors clearly show a divergent behavior to infinity with finer mesh either at general *k*-points [Fig. S2(a)] or high-

symmetry *k*-points [Fig. S2(b)], which are in good agreements with the theories. The line shapes of *Q* factors [Fig. S2(a)] are analogous to those of PTMMs with additional higher order complex Fourier components [Figs. S2(c) and S2(d)], indicating that finite *Q* factor dispersions are only affected and limited by the higher order complex Fourier components introduced by the finite size of meshes in our simulations. Similarly, the full-*k*-space *Q* factors of the PTMMs in the diffraction region (0, −1) are diverging to infinity with finer meshes as well, as shown in Fig. S3.

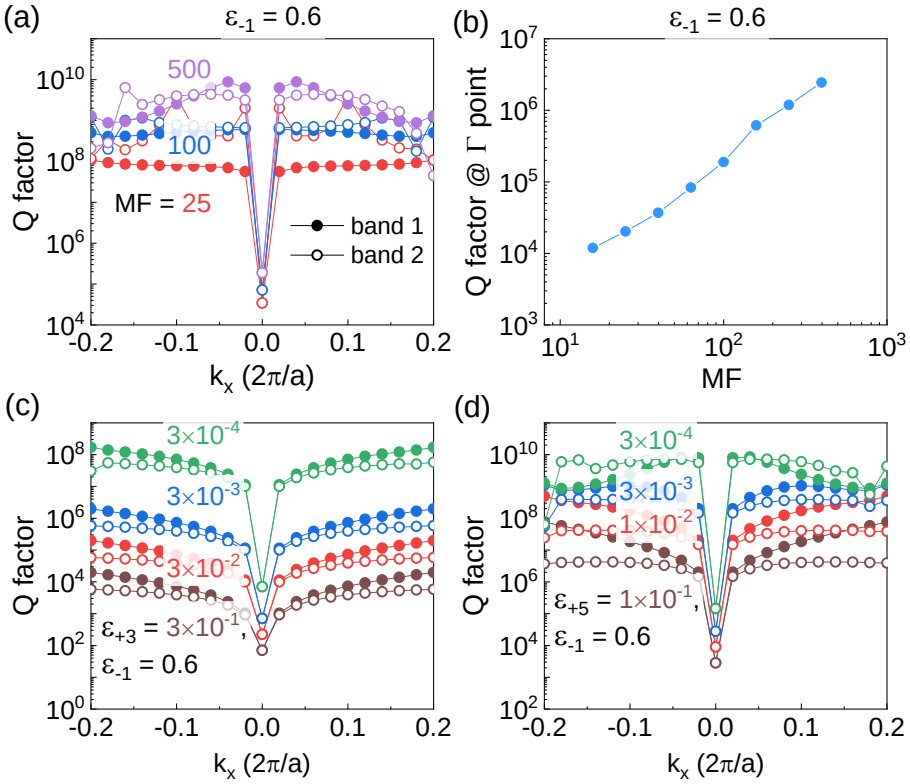

Fig. S2. Divergence of simulated *Q* factors and finite-element effects. (a) Simulated *Q* factors of band 1 and band 2 in Fig. 2 with various mesh fineness. The mesh factor (MF) is defined as the ratio of the period *a* to the maximum mesh size in the simulations. (b) *Q* factors of band 1 at the Γ point, clearly showing a divergence to infinity. (c) and (d) *Q* factors of band 1 and band 2 corresponding to PTMMs with additional high-order CFCs ε_{+3} (c) and ε_{+5} (d), showing a divergence to infinity with smaller high-order CFCs. The similar behavior with that of (a) indicates that the finite *Q* factors are merely limited by the finite size of meshes which introduce high-order CFCs.

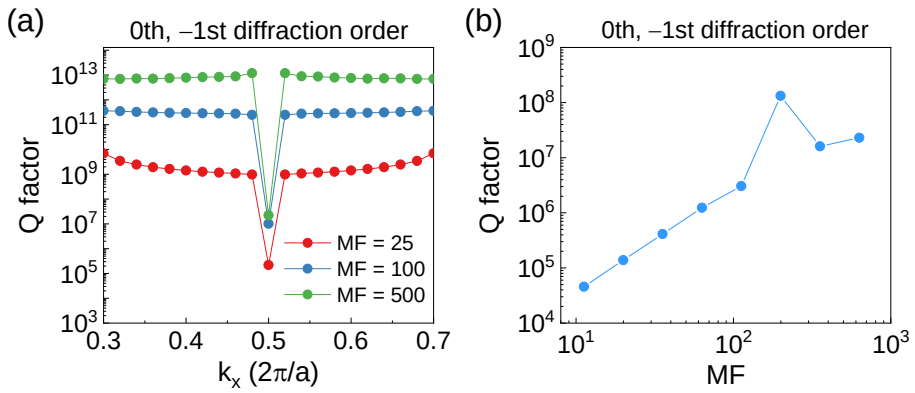

Fig. S3. Divergence of *Q* factors to infinity with finer meshes in the vicinity of the 3rd stopband. (a) *Q* factors of band 2 at the (0, –1) diffraction region in the vicinity of the third stopband, diverging with finer MFs. (b**)** *Q* factors of band 2 at the X point with finer meshes, clearly showing a divergence to infinity.

IV. Manipulation of the absolute lasing amplitudes

In this section we show that the *Q* actors and lasing amplitudes can be arbitrarily enlarged by tuning the PT perturbation depth of the PTMMs. At the resonance, the near-field enhancement $|E/E_0|$ is associated with the radiative *Q* factors (intrinsic loss is neglected) [2]:

$$\left|\frac{E}{E_0}\right|^2 \propto \frac{Q}{V_{eff}}, \tag{S26}$$

where E_0 is the amplitude of the incident plane-wave and V_{eff} is the effective mode volume. We treat the PT modulations as perturbations since the modulation depths are relatively small compared to the permittivity of the homogeneous slab. Therefore, the relative near field distributions are considered invariant and the diffraction power is proportional to the near-field enhancement: $R/T \propto \left|E/E_0\right|^2$. V_{eff} is invariant as well with the PT perturbations because the spatial localizations of the resonant modes are considered unchanged. Combining equations (S22) and (S23), the coefficients h_{-1} and h_{+3} show linear and cubic dependence of the overall PT modulation depth ε_{PT}, respectively. Therefore, the *Q* factors at high-symmetry *k*-points are clearly inverse quadratic to ε_{PT} since the eigenstate loss is known from equation (S24):

$$Q \propto 1/\sqrt{h_{-1}h_{+3}} \propto \varepsilon_{PT}^{-2}. \tag{S27}$$

Combining with equation (S26), we then get the scaling law of the lasing power at the resonances of quasi-EP-BICs:

$$R/T \propto Q \propto \varepsilon_{PT}^{-2}. \tag{S28}$$

The diffraction lasing strengths are predicted to be linear with the Q factors and be inverse quadratic to the overall PT modulation depth ε_{PT}. The characteristic inverse quadratic dependence is typical for quasi-BICs spawned from symmetry-protected BICs [3], indicating that the high-order CFCs of the D-PTMMs introduce full-k quasi-BICs.

To further consolidate our theory, we illustrate the simulated lasing strengths with different overall modulation depths ε_{PT} of the D-PTMMs in Figs. S4(a)–S4(e). One can clearly see that the line shapes are invariant but show amplified amplitudes at the resonances with larger PT modulation depths. Fig. S4(f) summarizes the scaling laws of the resonant diffraction strengths and the corresponding Q factors supported by the D-PTMMs, showing good agreements with the theory. Therefore, the absolute informational lasing amplitudes can be engineered by tuning the PT perturbation depth of the PTMMs.

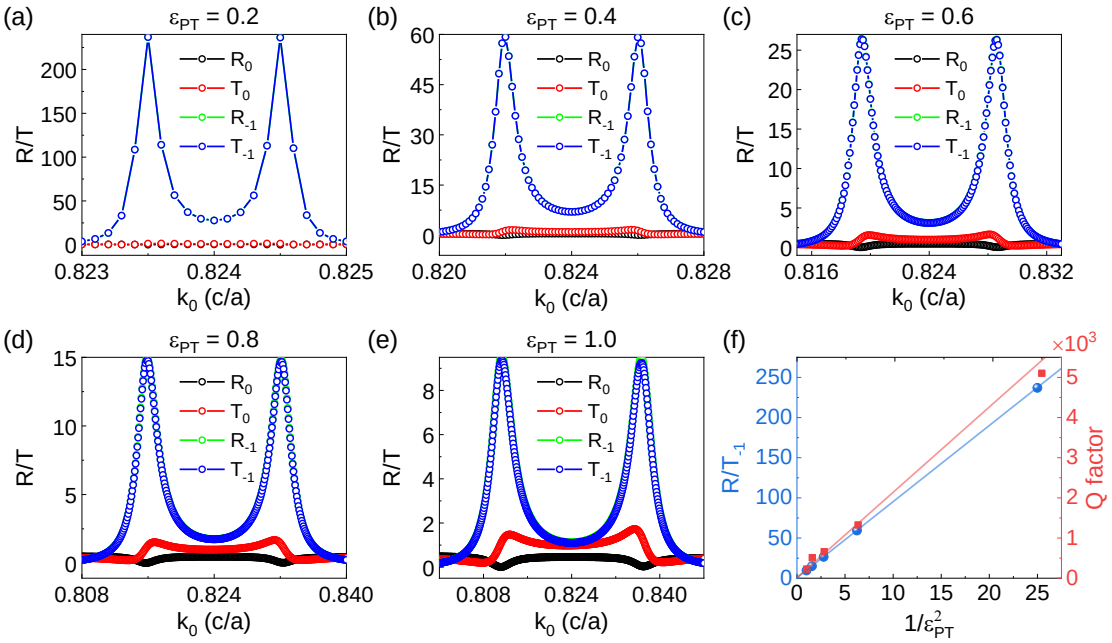

Fig. S4. Absolute lasing amplitudes engineering of the PTMMs. (a)–(e)**,** Diffraction strengths of the D-PTMMs with the overall modulation depth ε_{PT} = 0.2, 0.4, 0.6, 0.8, and 1.0, respectively. The illustrated D-PTMMs are in 0th, −1st diffraction order with an oblique incidence ($k_x = \pi / a$). (f) Scaling laws of the diffraction lasing strengths at the resonances of quasi-EP-BICs ($R/T \propto Q \propto \varepsilon_{PT}^{-2}$), which are proportional to the Q factors and inverse quadratic to the PT modulation depth ε_{PT} . Dots: simulation data; lines: theory.

V. Comprehensive spatial information lasing by configuring CFCs of permittivity

We demonstrate the ability to design arbitrary amplitudes and phases of different lasing Fourier components by illustrating representative PTMM configurations. Figure S5(a) shows the relative phase engineered by a PTMM with −2nd- and +3rd-order CFCs. As a proof of concept, we illustrate the spatial information lasing with three independent lasing channels (E_{rad}^{0} , E_{rad}^{-1} , E_{rad}^{-2}) operating in the vicinity of the 4th stopband with incident in-plane momentum $k_x = 2\pi / a$. The 0th-order lasing wave E_{rad}^{0} is invariant. E_{rad}^{-1} and E_{rad}^{-2} can cover the phases of 0 to 2π and 0 to 4π respectively, when we tune the phase of the 2nd-order CFCs ϕ_{-2} from 0 to 2π. In addition to phase manipulation of informational lasing, we can realize complex modulation of lasing

amplitudes and phases based on the correspondence between the CFCs $\varepsilon_{\pm n}$ and lasing fields E_{rad}^{m}, as shown in Fig. S5(b).

Furthermore, we demonstrate the characteristic lasing information entropy and lasing patterns from $\mathcal{S}$ = 0.10 to $\mathcal{S}$ = 0.53 and their corresponding PT modulations in Fig. S6. Generally, resulting from the modulation of unidirectional Bragg couplings inside the high-Q nanolaser cavity, we can obtain arbitrary spatial information by configuring the CFCs of the PTMMs, without additional optical components.

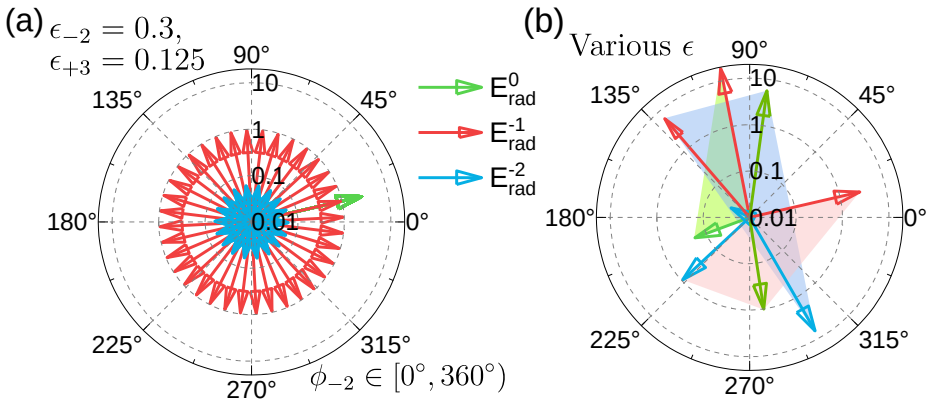

Fig. S5. (a) Phase and (b) amplitude engineering of multiple lasing Fourier components. The total lasing fields are completely controllable since the complex amplitude of each Fourier component can be manipulated. Shading areas in (c) denote various PTMM configurations.

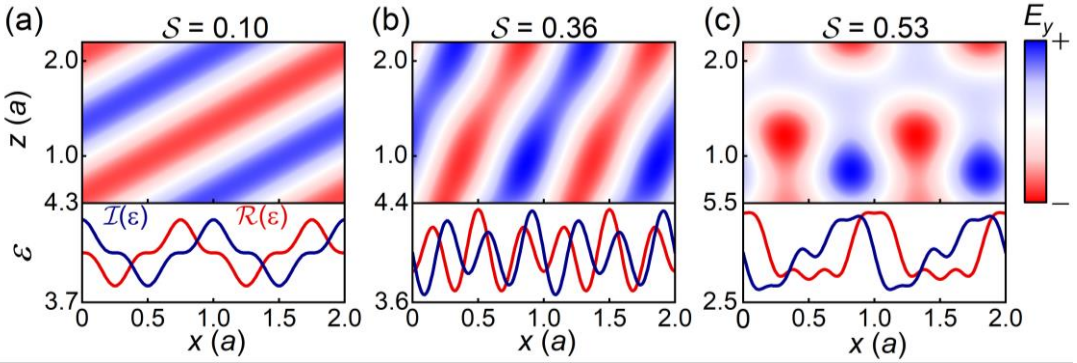

Fig. S6. Lasing information entropies, corresponding lasing patterns and CFCs. The CFCs configurations are: (a) $\varepsilon_{-1} = 0.15,\ \varepsilon_{+3} = 0.05$, (b) $\varepsilon_{-2} = 0.10,\ \varepsilon_{+3} = -0.25$, and (c) $\varepsilon_{-1} = 1.00,\ \varepsilon_{-2} = 0.40,\ \varepsilon_{+4} = -0.20$, with ε_0 fixed at 4. The principles of full-k BICs are compatible with numerous CFC configurations, which leads to on-demand informational lasing.

VI. Mode (*k*-mode) competition analysis by laser rate equations

The mode competition between FGM and BGM is trivial except for in the vicinity of high-symmetry *k*-points (degenerate points, EP-BIC points), because their free spectrum range (FSR) at general *k*-points is generally larger than the full width at half maximum (FWHM) of the gain spectrum (single-mode lasing can be achieved by gain dispersion as modes are dispersive). Therefore, we discuss mode competitions between (1) a pair of counter-propagating guided modes in the vicinity of degenerate points; (2) modes belong to one band with close but different *k* and eigenfrequencies, by rate equation analysis. We argue that both single-mode and single-*k*-mode lasing can be achieved.

(1) Counter-propagating guided mode competitions

Considering the linear and nonlinear couplings, the coupled rate equations for the two counter-propagating guided modes $E_1(t)$ and $E_2(t)$ read [4–6]

$$\frac{dE_1}{dt} = \kappa(1+i\alpha)[N(1-s|E_1|^2-c|E_2|^2)-1]E_1 - \kappa_1 E_2, \tag{S29}$$

$$\frac{dE_2}{dt} = \kappa(1+i\alpha)[N(1-s|E_2|^2-c|E_1|^2)-1]E_2 - \kappa_2 E_1, \tag{S30}$$

$$\frac{dN}{dt} = \gamma[\mu - N - N(1-s|E_1|^2-c|E_2|^2)|E_1|^2 - N((1-s|E_2|^2-c|E_1|^2)|E_2|^2], \tag{S31}$$

where $E_1(t)$ and $E_2(t)$ are the slowly-varying normalized amplitudes of forward and backward propagating guide modes, N is the carrier density, κ is the field decay rate, γ is the decay rate of the carrier population,α is the linewidth enhancement factor, μ is the normalized injection current ($\mu = 0$ at transparency, $\mu \approx 1$ at the lasing threshold), $\kappa_{1,2}$ denotes the linear mode couplings arising from the Bragg scattering of the PT-modulated grating, c and s are the nonlinear couplings of guided modes resulting from gain saturation on their own and by each other, respectively.

The linear mode coupling coefficients $\kappa_{1,2}$ are determined by the Bragg scattering of the CFCs of the PTMMs, which is approximately zero in the absence of the grating modulation, and is symmetric (asymmetric) when the grating is index gratings (PT-modulated gratings).

The nonlinear coupling of guided modes arises from gain saturation. The self-saturation and inter-mode saturation through spectral hole burning and carrier heating effects are described by the *s* and *c* saturation parameters [4]. Carrier density pulsation effects is neglected since the guided modes have a spatial period much smaller than the

carrier diffusion length [5].

We numerically solved the rate equations by the standard 4th-order Runge-Kutta method, and extract the steady-state electric field amplitudes to plot the bifurcation diagrams. As an illustrative system, we use the parameters of the resemble semiconductor PT-symmetric micro-ring laser [4]: $\kappa = 100\ \mathrm{ns}^{-1}$, $\gamma = 0.2\ \mathrm{ns}^{-1}$, $\alpha = 3.5$, and $c = 2s = 0.01$.

To show the mode selection of the PTMMs operating close to the EPs, we chose various values of linear mode couplings $\kappa_{1,2}$ and plotted the bifurcation diagram of the equations (maximum and minimum of the amplitude $|E_{1,2}(t)|$ versus the normalized injection current μ). Without gratings, $\kappa_{1,2}$ typically take a small and equal value, $\kappa_1 = \kappa_2 = \kappa_d + i\kappa_c$ arising from spurious backscattering in the semiconductor waveguide [4,5]. The linear coupling is completely asymmetric at EPs, i.e., $\kappa_2/\kappa_1 = 0$ for the sinusoidal PTMMs. One gets non-vanishing small κ_2/κ_1 in the vicinity of EPs with unbalanced real and imaginary modulations.

As shown in Fig. S7(a), the bifurcation diagram with $\kappa_1 = \kappa_2 = \kappa_d + i\kappa_c$ shows different dynamics, namely, symmetric continuous-wave (CW) bidirectional emission (region I), alternating mode oscillations (region II), and unidirectional bistable CW emission (region III), in consistence with previous works [4]. The BGM E_1 and the FGM E_2 share the same lasing features with symmetric couplings ($\kappa_1 = \kappa_2$). As the sinusoidal PT-modulation is gradually approached ($\kappa_2/\kappa_1 \rightarrow 0$), the BGM E_1 is dominating over the FGM E_2, with larger and larger amplitudes than E_2, as shown in Figs. S7(b) and S7(c). The region of alternating oscillations shrinks from Fig. S7(b) to S7(c), indicating the mode E_1 plays a more dominant role in lasing process as well. At the EP-BIC condition $\kappa_2/\kappa_1 = 0$, the FGM E_2 is fully suppressed and the laser operates unidirectionally in a stable CW regime, as shown in Fig. S7(d). The laser rate equation analysis clearly indicates that operation of the full-k BICs lasing in the vicinity of EPs is robust and stable to achieve single-mode laser oscillation.

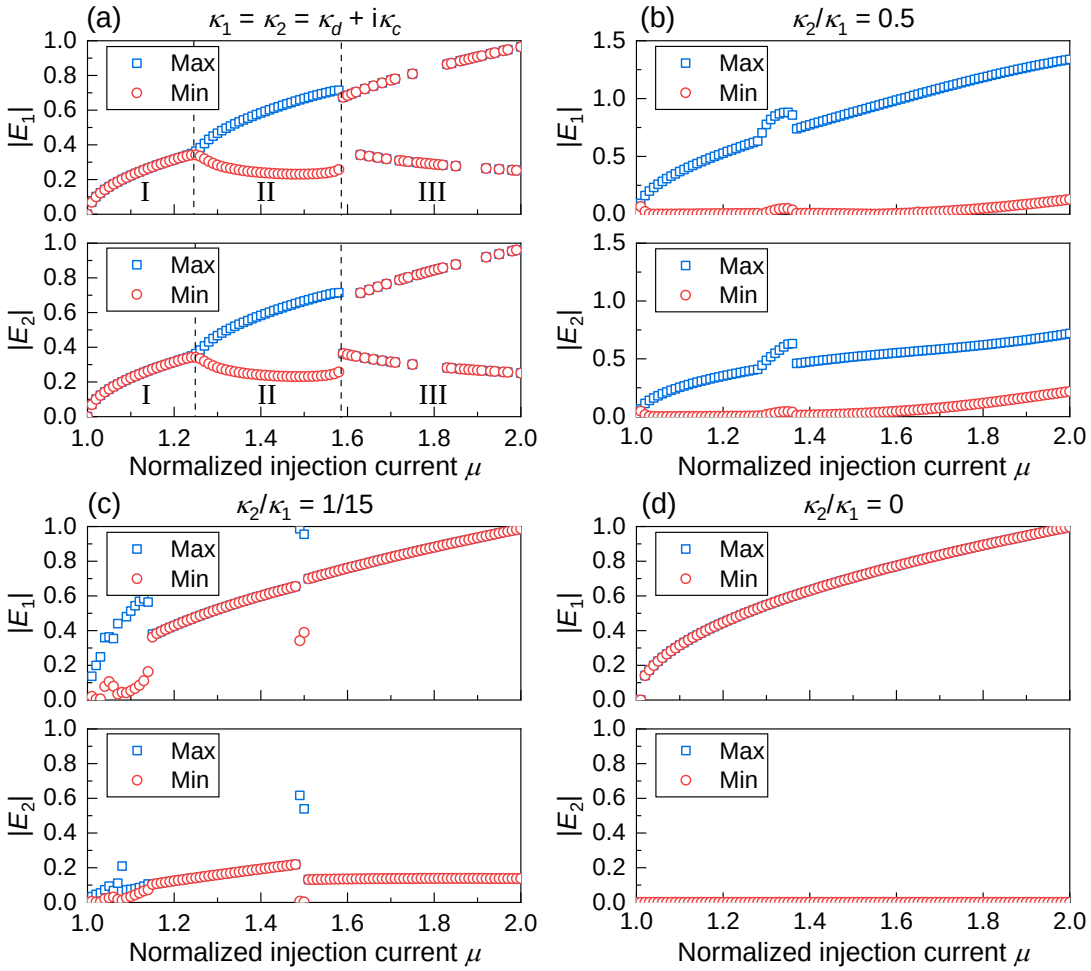

Fig. S7. Bifurcation diagrams of the semiconductor laser rate equations, depicting the maximum and minimum of the amplitude $|E_{1,2}(t)|$ versus the normalized injection current μ ($\mu = 1$ at the threshold), for different values of linear mode couplings κ_1 and κ_2. (a) $\kappa_1 = \kappa_2 = \kappa_d + i\kappa_c$, $\kappa_c = 0.44$ ns^{-1}, $\kappa_d = 0.0327$ ns^{-1}, corresponding to weak backscattering and absence of the grating modulations. (b) Highly unbalanced index and loss/gain gratings ($\kappa_1 = 5i$ ns^{-1}, κ_2/κ_1=0.5). (c) Slightly unbalanced real and imaginary modulation gratings ($\kappa_1 = 5$i ns^{-1}, κ_2/κ_1=1/15). (d) EP-BIC condition of sinusoidal PT-modulated gratings ($\kappa_1 = 5$i ns^{-1}, $\kappa_2/\kappa_1 = 0$).

(2) *k*-mode competitions

Different *k*-modes resemble various longitudinal modes of quasi-periodic Fabry-Perot (FP) cavity with large enough size. The couplings among the longitudinal modes should abbey conservation of both energy and momentum. The longitudinal modes can be directly coupled by four-wave mixing in semiconductor FP lasers [7], but the carrier density grating effect is often neglected when one considers mode competitions close to the lasing threshold [6,8,9]. Therefore, each one of the *k*-modes becomes an

independent oscillator, and the inter-coupling terms in the rate equation are dropped.

Similarly, the rate equations for the two close k-modes $E_{k1}(t)$ and $E_{k1}(t)$ with plan-wave seeding injection read [10,11]

$$\frac{dE_{k1}}{dt} = \kappa(1+i\alpha)[N(1-s|E_{k1}|^2-c|E_2|^2)-1]E_{k1} - \kappa_{\text{ext1}}E_{\text{ext}}, \quad \text{(S32)}$$

$$\frac{dE_{k2}}{dt} = \kappa(1+i\alpha)[N(1-s|E_{k2}|^2-c|E_{k1}|^2)-1]E_{k2} - \kappa_{\text{ext2}}E_{\text{ext}}, \quad \text{(S33)}$$

$$\frac{dN}{dt} = \gamma[\mu - N - N(1-s|E_{k1}|^2-c|E_{k2}|^2)|E_{k1}|^2 - N((1-s|E_{k2}|^2-c|E_{k1}|^2)|E_{k2}|^2], \text{(S34)}$$

where $E_{k1}(t)$ and $E_{k2}(t)$ are the slowly-varying normalized amplitudes of two close k-modes $E_{k1}(t)\varphi(x)e^{-i(\omega_1 t - k_1 x)}$ and $E_{k2}(t)\varphi(x)e^{-i(\omega_2 t - k_2 x)}$ belong to one band, E_{ext}(t) is the injected amplitude of plane-wave seeding injection, and $\kappa_{\text{ext1,2}}$ are the couplings between injected seeding E_{ext} and mode $E_{k1,k2}$.

The plane-wave seeding injection $E_{ext}(t)e^{-i(\omega_1 t - k_x x - k_y y)}$ shares the same frequency ω_1 with mode E_{k1} and can be unidirectionally scattered to E_{k1} by the Bragg process: $k_1 = k_x - G$ (G is the reciprocal lattice vector), while couplings between E_{ext} and E_{k2} do not satisfy energy and momentum conservation. The external couplings κ_{ext1} and κ_{ext2} show great difference since the E_{k1} mode has larger in-plane momentum overlapping and spectral overlapping, i.e., $\kappa_{\text{ext2}}/\kappa_{\text{ext1}} \rightarrow 0$.

To show the robust k-mode selection by the plane-wave seeding injection, we plot the bifurcation diagram with various coupling difference $\kappa_{\text{ext2}}/\kappa_{\text{ext1}}$. As shown in Fig. S8(a), the two k-modes show identical behaviors with symmetric continuous-wave (CW) bidirectional emission (region I) and unidirectional bistable CW emission (region III), manifesting severe mode competitions with symmetric seeding couplings. However, mode E_{k1} dominates over mode E_{k2} with slightly external coupling difference ($\kappa_{\text{ext2}}/\kappa_{\text{ext1}} = 0.99$), as shown in Fig. S8(b). The mode E_{k2} is further suppressed in lasing when $\kappa_{\text{ext2}}/\kappa_{\text{ext1}} = 0.5$ [Fig. S8(c)]. Single-k-mode lasing of E_{k1} is achieved and mode E_{k2} is fully suppressed at completely asymmetric external coupling condition ($\kappa_{\text{ext2}}/\kappa_{\text{ext1}} = 0$), as shown in Fig. S8(d). This is intuitive since the mode E_{k1} starts lasing from seeding photons while the mode E_{k1} from quantum noise. Therefore, robust single-k-mode lasing can be achieved with a plan-wave seeding injection.

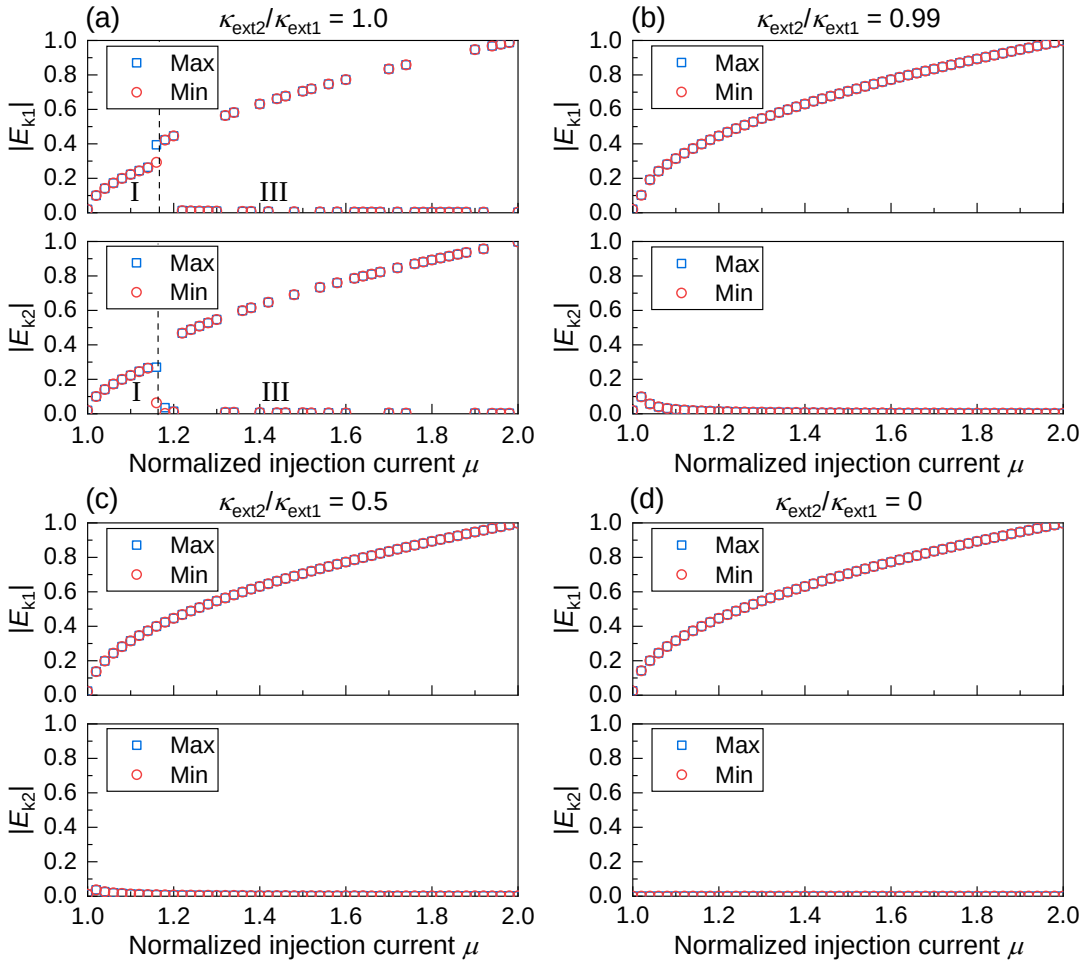

Fig. S8. Bifurcation diagrams of the semiconductor laser rate equations, depicting the maximum and minimum of the amplitude $|E_{k1,2}(t)|$ versus the normalized injection current μ (μ = 1 at the threshold), for different values of external couplings κ_{ext1} and κ_{ext2}. The amplitude of seeding injection E_{ext} is set as 0.01. (a) $\kappa_{ext1} = \kappa_{ext2} = 0.5i$ ns^{-1}, corresponding to symmetric external seeding injection. (b) Slightly asymmetric external couplings ($\kappa_{ext1} = 0.5i$ ns^{-1}, $\kappa_{ext2}/\kappa_{ext2} = 0.99$). (c) Highly asymmetric external couplings ($\kappa_{ext1} = 0.5i$ ns^{-1}, $\kappa_{ext2}/\kappa_{ext2} = 0.5$). (d) Completely asymmetric external couplings ($\kappa_{ext1} = 0.5i$ ns^{-1}, $\kappa_{ext2}/\kappa_{ext2} = 0$). Other simulation parameters are the same as Fig. S7.

VII. Feasible protocols and error analysis

As illustrated in Fig. S9, the specific optical constant profile can be discretized and realized by an index-contrast grating according to the effective medium theory (see results in Fig. 3), no necessity for a continuous control of complex Fourier components (CFCs). We noticed that resemble CFC manipulations have been realized by some

research groups. For example, Feng *et al*. have reported the experiments with similar control depth and precision of CFCs (Fig. 2b in Ref. [12]), including both gain and loss manipulation using silicon-based metamaterial. Wong *et al.* realized lasing and anti-lasing PT-symmetry-modulated waveguide (first paragraph on page 797 and Fig. 1 in Ref. [13]). Besides the optical waveband region, CFCs modulation can also be realized in long-wave band such as microwave with more accuracy and flexibility. We believe the required CFCs are experimentally attainable according to corresponding reports. But the fabrication of such metamaterial is beyond the current fabricating technique in our group. Recently, we are trying to upgrade our laboratory to reach the required fabrication conditions.

The main challenge of the specific optical constant profiles can be summarized as three aspects: (1) The modulation depth/range compared to average optical constants ($\Delta\varepsilon_{r,i}/\varepsilon_{ave}$); (2) The maximum spatial gradient of optical constants that determines high-order CFCs ($\nabla\varepsilon_{r,i}$); (3) The robustness of system parameters on the information entropy. Table S1 compared conditions (1) and (2) between our work and pioneering experimental schemes involving CFC modulations, showing that the required CFCs are basically attainable. Our CFC configurations are comparable with various recent works as well [16–18].

As the system gain can be adjusted to match the loss by altering the pump power, we examine the errors in the calculated information entropy Σ caused by out-of-plane parameters (thickness) and in-plane parameters (imbalance of real/imaginary modulation), as depicted in Fig. S10.

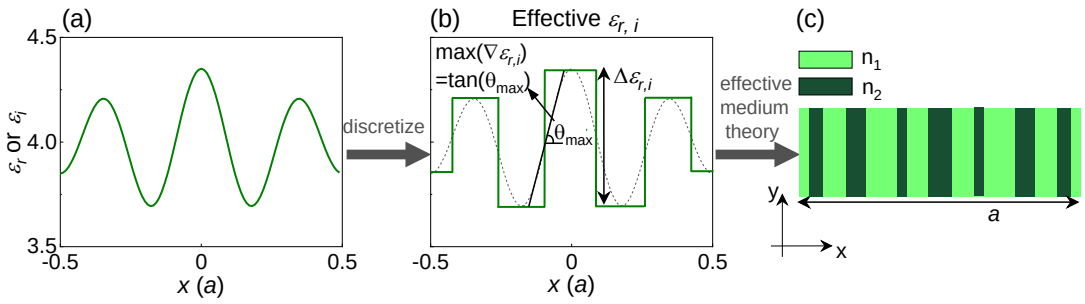

Fig. S9. Schematic of optical constant profile discretization. The permittivity profile can be discretized and further realized by index-contrast gratings according to the effective medium theory. *a* is the modulation period.

Table S1. CFC parameter comparison between full-*k*-BICs and pioneering experimental publications

Ref.	System	$\varepsilon_{r,i}$ / ε_{ave}	Period *a*	max($\nabla\varepsilon_{r,i}$)	Operating wavelength
[12]	Metamaterial	11.1%	140 nm	9.0E-3 nm^{-1}	~1550 nm
[13]	Waveguide	0.2%	250 nm	6.0E-6 nm^{-1}	1556 nm
[14]	Micro ring	Perturbation	~500 nm	NAN	~1550 nm
[15]	Micro ring	0.6%	~500 nm	4.0E-5 nm^{-1}	~1550 nm
This work	Metamaterial	~0 – ~10%	Dimensionless, e.g., 800 nm	Dimensionless, e.g., 3.1E-3 nm^{-1} for Fig. 2 2.0E-3 nm^{-1} for Fig. 3	Dimensionless, e.g., 1550 nm

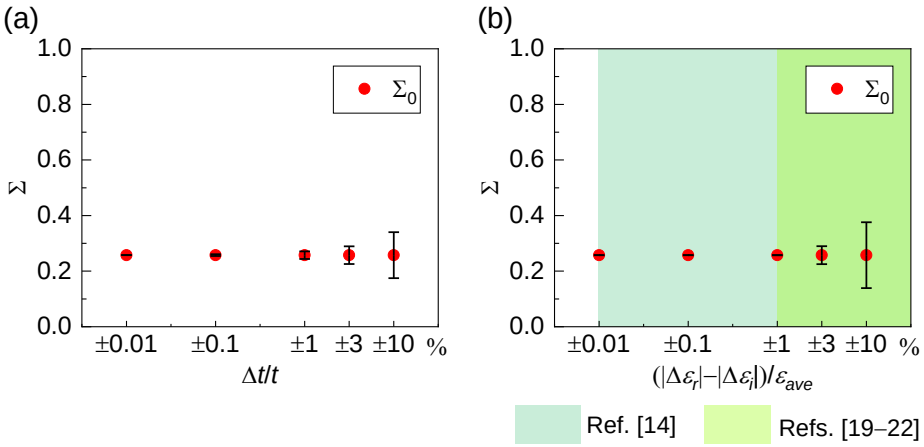

Fig. S10. Robustness of the calculated information entropy, in respect of (a) relative thickness difference $\Delta t / t$, (b) relative imbalance of real/imaginary modulation $(|\Delta\varepsilon_r| - |\Delta\varepsilon_i|) / \varepsilon_{ave}$. Match of gain and loss can be easily achieved by altering the pump power. The dot represents the true value of Σ without parameter errors (Σ_0), while the error bar represents the deviation of Σ with parameter errors.

VIII. Full-*k* BICs versus lasing threshold modes

We would like to identify the proposed full-*k* BICs from the lasing threshold modes reported by Ref. [17]. Full-*k*-BICs of band 2 (band 3) shows perfect destructive interference of leaky waves while BICs of band 3 (band 2) originates from balancing near-field gain and losses of radiative waves when the in-plane wavevector $0 < k_x < \pi / a$ ($\pi / a < k_x < 2\pi / a$), as shown in Figs. S11(a) and S11(b). The eigenstates with infinite Q factor as a result of balanced gain and loss were labeled as lasing threshold modes [17]. All bands show destructive interference of radiation waves at the high-symmetric *k*-points. We further calculated the far-field radiative power P_{rad}

($P_{rad} = \int_S \mathbf{S}_{rad} \cdot \mathbf{n} dS$, where $\mathbf{S}_{rad}$ is the radiative time-averaged Poynting vector) and the near-field absorption power P_{abs} ($P_{abs} = \frac{1}{8\pi} \int_V \omega \, \mathrm{Im}(\varepsilon) |\mathbf{E}|^2 \, dV$, integrating the volume of the PTMMs V) of band 2 and band 3 [Figs. S11(c) and S11(d), respectively]. The full-k BICs of band 2 (band 3) have both zero radiations and absorptions while band 3 (band 2) manifests non-zero P_{abs} with $P_{abs} = -P_{rad}$ when $0 < k_x < \pi / a$ ($\pi / a < k_x < 2\pi / a$). All bands show zero radiations and absorptions at the high-symmetric k-points. Therefore, one of the counter-propagating guided modes is the lasing threshold mode while the other one mode is the general BIC at the general k-points, and all modes are general BICs at the high-symmetric k-points.

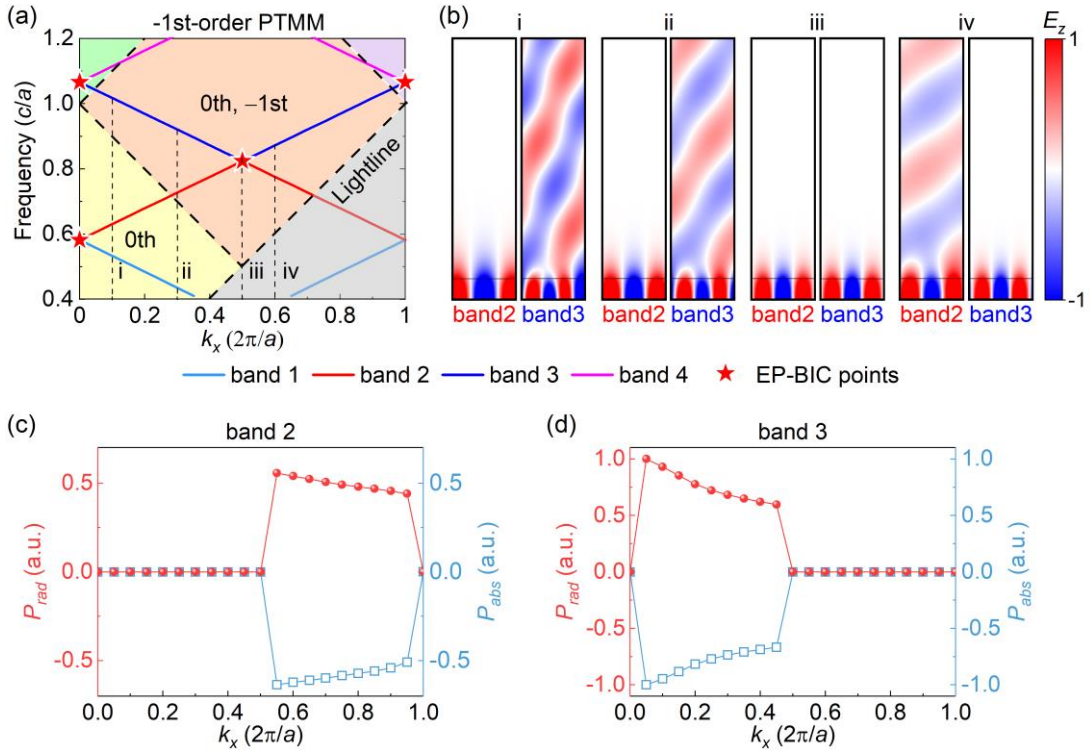

Fig. S11. (a) Band dispersions of -1st-order PTMM manifesting full-k-space BICs and (b) the corresponding eigenstate fields. (c) and (d) The far-field radiative power P_{rad} and the near-field absorption power P_{abs} of full-k-BIC band 2 and band 3, respectively. The negative absorption means net gain.

References

[1] S.-G. Lee, S.-H. Kim, and C.-S. Kee, Phys. Rev. Lett. **126**, 013601 (2021).

[2] Y. Liang, K. Koshelev, F. Zhang, H. Lin, S. Lin, J. Wu, B. Jia, and Y. Kivshar, Nano Lett. **20**, 6351 (2020).

[3] K. Koshelev, S. Lepeshov, M. Liu, A. Bogdanov, and Y. Kivshar, Phys. Rev. Lett. **121**, 193903 (2018).

[4] M. Sorel, P. J. R. Laybourn, A. Scirè, S. Balle, G. Giuliani, R. Miglierina, and S. Donati, Opt. Lett. **27**, 1992 (2002).

[5] M. Sorel, G. Giuliani, A. Scire, R. Miglierina, S. Donati, and P. J. R. Laybourn, IEEE J. Quantum Electron. **39**, 1187 (2003).

[6] I. Stamataki, S. Mikroulis, A. Kapsalis, and D. Syvridis, IEEE J. Quantum Electron. **42**, 1266 (2006).

[7] X. Cai, Y. L. D. Ho, G. Mezosi, Z. Wang, M. Sorel, and S. Yu, IEEE J. Quantum Electron. **48**, 406 (2012).

[8] L. Tien-Pei, C. Burrus, J. Copeland, A. Dentai, and D. Marcuse, IEEE J. Quantum Electron. **18**, 1101 (1982).

[9] Y. Ting and D. Welford, IEEE J. Quantum Electron. **22**, 2116 (1986).

[10] M. Schell, W. Utz, D. Huhse, J. Kässner, and D. Bimberg, Appl. Phys. Lett. **65**, 3045 (1994).

[11] G. Yuan and S. Yu, IEEE J. Quantum Electron. **44**, 41 (2008).

[12] L. Feng, Y.-L. Xu, W. S. Fegadolli, M.-H. Lu, J. E. B. Oliveira, V. R. Almeida, Y.-F. Chen, and A. Scherer, Nat. Mater. **12**, 108 (2013).

[13] Z. J. Wong, Y. L. Xu, J. Kim, K. O'Brien, Y. Wang, L. Feng, and X. Zhang, Nat. Photonics **10**, 796 (2016).

[14] L. Feng, Z. J. Wong, R. M. Ma, Y. Wang, and X. Zhang, Science **346**, 972 (2014).

[15] P. Miao, Z. Zhang, J. Sun, W. Walasik, S. Longhi, N. M. Litchinitser, and L. Feng, Science **353**, 464 (2016).

[16] W. Wang, L.-Q. Wang, R.-D. Xue, H.-L. Chen, R.-P. Guo, Y. Liu, and J. Chen, Phys. Rev. Lett. **119**, 077401 (2017).

[17] Q. Song, J. Hu, S. Dai, C. Zheng, D. Han, J. Zi, Z. Q. Zhang, and C. T. Chan, Sci. Adv. **6**, eabc1160 (2020).

[18] Y. Xu, L. Li, H. Jeong, S. Kim, I. Kim, J. Rho, and Y. Liu, Sci. Adv. **9**, eadf3510 (2023).

[19] R. Yao, C.-S. Lee, V. Podolskiy, and W. Guo, Laser Photonics Rev. **13**, 1800154 (2019).

[20] K.-H. Kim, M.-S. Hwang, H.-R. Kim, J.-H. Choi, Y.-S. No, and H.-G. Park, Nat. Commun. **7**, 13893 (2016).

[21] L. Feng, M. Ayache, J. Huang, Y.-L. Xu, M.-H. Lu, Y.-F. Chen, Y. Fainman, and A. Scherer, Science **333**, 729 (2011).

[22] M. P. Hokmabadi, N. S. Nye, R. El-Ganainy, D. N. Christodoulides, and M. Khajavikhan, Science **363**, 623 (2019).